©Copyright 2013

G. Wayne Stewart

Ancient playa in Glenelg Region, Gale Crater, Mars: evidence derived from the polygonal flagstone network in mudstone imaged by Curiosity

G. Wayne Stewart

A thesis submitted in partial fulfillment of the requirements

for the degree of

Master of Science

University of Washington

2013

Committee:

Bernard Hallet

Ronald S. Sletten

Program Authorized to Offer Degree:

Earth and Space Sciences

University of Washington

Abstract

Ancient playa in Glenelg Region, Gale Crater, Mars: evidence derived from the polygonal flagstone network in mudstone imaged by Curiosity

G. Wayne Stewart

Chair of the Supervisory Committee:

Prof. Bernard Hallet

Earth and Space Sciences

Polygonal patterned surfaces (PPS) are common on Mars, and found in the Glenelg region of Gale Crater that was extensively studied with the Curiosity rover in the first 200 sols of the Mars Science Laboratory (MSL) mission. PPS can form by various mechanisms that lead to volumetric contraction of the regolith, sediments, or bedrock. It is hypothesized that a network of contraction fractures formed at Glenelg as the fine-grained clay-rich sediment lost moisture, and produced the distinct array of widely spaced flagstones approaching one meter in width evident in images from Curiosity. This study suggests that Glenelg PPS is not the product of thermal contraction of

permafrost as noted elsewhere on Mars. The uniform distributions of fracture orientation and spacing between flagstones, large volumetric contraction, fine-grained texture of the sediments, and presence of swelling clays are all consistent with the PPS forming in a drying playa. These findings are in agreement with diverse, recent studies suggesting that Glenelg is a former lake bed at the base of an alluvial fan. This would imply that Glenelg PPS formed when the surface temperature and air pressure supported liquid water, and allowed temporary playa conditions of sufficient duration to permit ponding, sediment accumulation, and desiccation.

TABLE OF CONTENTS

Page

LIST OF FIGURES

Figure Number Page

LIST OF TABLES

ACKNOWLEDGMENTS

I am grateful for the guidance of my advisors, Professors Bernard Hallet and Ronald Sletten, and for computing assistance from Harvey Greenberg and Ed Mulligan. My thanks to Paul Sampson for his review of the study's statistical techniques, to Charlotte Schreiber for sharing some of her insights about sediments from arid regions, to Mike Malin for admitting me into the Mars Laboratory Science Team as a research collaborator, and to David Bish and Kurt Lawson for permission to use their photographs.

DEDICATION

To Matthew and Marybeth

1. Introduction

Networks of polygonal surface features are widespread on Mars. They are commonly observed from polar cap latitudes to approximately 30° latitude [Mutch et al., 1977; Malin and Edgett, 2001; Kuzmin and Zabalueva, 2003; Mangold, 2005; Kostama et al., 2006; Levy et al., 2010], and less frequently at equatorial latitudes [El Maarry, 2010]. The processes forming martian polygons have been discussed since the Viking 2 lander set down amidst polygon troughs at 48.3° N, 226.0° E in 1976 [Mutch et al., 1977; Pechmann, 1980; Mellon, 1997; Seibert and Kargel, 2001; Mellon et al., 2009b]. Thermal contraction of permafrost and desiccation of sediment were two formative processes of great interest during the Viking 2 mission, and they continue to be of interest today.

Where networks of polygons are known to be the product of thermal contraction in permafrost regions on Earth, they are generally referred to as polygonal patterned ground (PPG) [Washburn, 1979]. For the distinct pattern of widely spaced flagstones in the Glenelg study area (Fig. 1) we use the term polygonal patterned surface (PPS) as it does not imply a specific formative mechanism; PPS appears very rarely in the literature, sometimes with reference to PPG [e.g., Mellon et al., 2008], and other times with reference to desiccation features [e.g., Howell et al., 2006]. In this paper only polygonal fracture patterns known to arise from thermal contraction of ice-rich permafrost will be described as PPG. All other polygonal patterns will be termed PPS.

Contraction, due either to cooling or desiccation, is the widely accepted underlying cause for PPS across Mars. Satellite imagery is inadequate, however, to

distinguish clearly between cooling or desiccation mechanisms [e.g., Mangold, 2005; El Maarry, 2010]. The wide distribution of PPS and the wide range of polygon diameters – from meter-scale to 10 km– suggest multiple formative processes, as well as the influence of varying site characteristics, including latitude and substrate properties. Moreover the results of these previous studies of satellite imagery cannot be applied to Glenelg PPS because the scale of Glenelg polygons, 0.5 m, is too small for clear satellite imaging. Only ground-level Curiosity imagery provides the resolution needed for a suitable study of the relatively small scale PPS at Glenelg.

Landed spacecraft provide diverse *in situ* data on PPS that complement satellite data. The landing sites of Viking 2 and Phoenix were located within martian PPS [e.g., Mutch et al., 1977; Mellon et al., 2009a]. No previous Mars rover had encountered PPS. The study reported here has the strong advantage over previous studies of having detailed images and diverse data obtained from the Curiosity rover at multiple sites of PPS within the Glenelg region of Gale Crater. This new information from Curiosity adds considerable motivation for this research by contributing to the emerging evidence that a lake once formed in the Glenelg region of Gale Crater [Dietrich et al., 2013], which is consistent with previous suggestions of fluvial activity on Mars [Irwin et al., 2005]. The lake would have contained sediment that, as it desiccated, formed the PPS photographed by the Curiosity rover. Within this conceptual framework, PPS at Glenelg is mainly the product of playa desiccation under surface temperature and atmospheric pressure allowing liquid water to be stable, at least for some period.

The morphology of Glenelg PPS will be characterized, and compared to that of other PPS on Mars and on Earth. Curiosity instrument data will be examined to test the

hypothesis that the PPS at Glenelg formed as a result of desiccation. Thermal contraction of permafrost and PPG formation will be considered in the Discussion section. It will be argued that the large volumetric contraction evident from the wide gaps between flagstones, and the flagstones' fine texture and presence of swelling clays (~20% smectite) collectively offer strong support for the desiccation hypothesis.

1.1. Background

A simple hypothesis for the network of evenly spaced polygonal flagstones that characterize Glenelg PPS is that they formed as contraction fractures developed in a continuous sediment layer. Contraction fractures are typically subvertical [Müller, 1998; Sletten et al., 2003], and where they intersect at the ground surface they can define networks of adjacent "polygons": two-dimensional, subhorizontal "closed figures bounded by several sides, some or all of which may be curved" [e.g., Lachenbruch, 1962].

While it is clear that most PPS and PPG are defined by fractures that form as surface-parallel stresses arise (due to the material contracting) and exceed the strength of the material, the dominant process responsible for the contraction is not obvious. Desiccation and cooling can produce similar polygonal patterns of fractures in fine-grained cohesive sediments and in permafrost, respectively (Figs. 1, 2, 3).

Figure 1. PPS with ~0.3 m polygons in a roadside mud puddle [courtesy of B. Hallet].

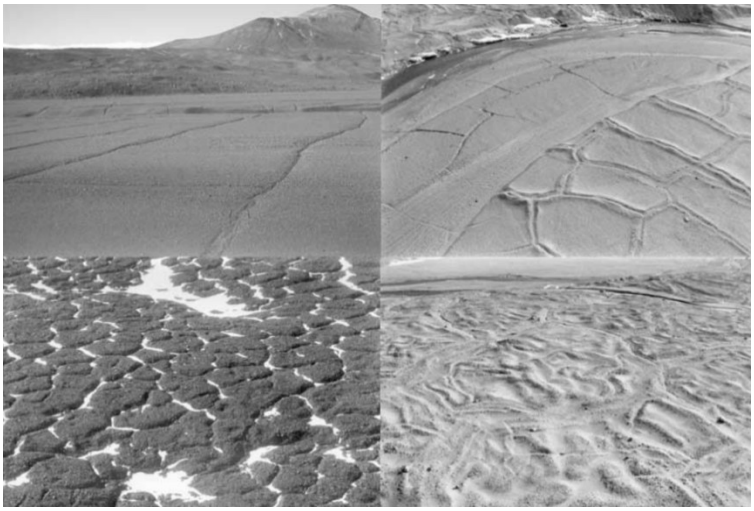

Figure 2. Antarctic PPG at different stages of development with polygon size ranging from 10 to 25 m. Upper left, initial stage, Taylor Valley. Upper right, initial and developing stages, Wright Valley. Lower left, mature stage, Beacon Valley. Lower right, complex PPG with non-uniform subsurface ice distribution, Wright Valley. From Sletten et al. [2003].

Figure 3. PPG, Victoria Valley, Antarctica. The sand-wedge polygons are approximately 20 m in size [Hallet et al., 2011].

Even if moisture loss is clearly responsible for the contraction and cracking, the causes of moisture loss may remain elusive. Loss of water can produce polygons subaerially in fine-grained sediment due to evaporation [Neal et al., 1968], or it can produce polygons subaqueously when an increase in salinity around fine-grained sediment causes water to be extracted from the sediment, a process known as synaeresis [Plummer and Gostin, 1981]. Where desiccation and synaeresis are both possible, considerable information about the formative environmental conditions would be needed to determine whether desiccation or synaeresis is responsible for the contraction fractures.

Moreover, desiccation PPS and thermal contraction PPG can be very similar in form and size [El Maarry et al., 2010; Müller, 1998]. Evaporation at the surface of fine-grained sediment or a drop in the water table can desiccate sediment [El Maarry et al., 2010]. Similarly, when the surface of ice-cemented permafrost cools, layer-parallel tensile stresses develop and increase until the permafrost fractures [Lachenbruch, 1962]. The similarity of fracture patterns for drying fine-grained sediment and cooling ice-cemented permafrost reflect the similarity in the underlying physics and fracture behavior; both materials are viscoelastic solids responding to volumetric contraction, with similar stress fields that cause and are, in turn, relieved by the fractures [Müller, 1998].

On Mars, at the smallest scale clearly visible from satellite, polygons of < 25 m size exhibit a variety of morphologies. Levy et al. [2010] organized small high-latitude (30–80°) polygons into seven morphological groups. They interpreted all morphological groups except one as PPG. The Phoenix lander provided *in situ* data with which to test this interpretation for one of the proposed permafrost morphological

group: flat-top small-polygon PPS. According to Levy et al. [2009], these data suggest PPS formed in ice-rich permafrost at the Phoenix landing site (68.2° N, 234.2° E). Mellon et al. [2008] modeled the stress field for permafrost at the Phoenix landing site latitude and noted that it was consistent with the 5 m-diameter polygons observed by Phoenix. There is strong consensus that permafrost processes form PPG today on Mars at high latitudes.

At lower latitudes the PPS formation process is ambiguous. El Maarry et al. [2010] analyzed crater floor polygons ranging in size from 15 to 350 m in Mars Orbiter Camera (MOC) and High Resolution Imaging Science Equipment (HiRISE) imagery. They found "a network of regularly spaced troughs surrounding an interior region of relatively level ground indicative of lake beds," featuring orthogonal, hexagonal and irregular intersection patterns. They used a viscoelastic model of thermal contraction to calculate the stress distribution in the martian ground, including the maximum tensile stress as a function of latitude. Following early studies of thermal contraction [e.g., Lachenbruch, 1962], stress was related to fracture depth and size of the zone of stress relief, which provided an estimate of maximum polygon size. At latitudes below 45° the modeled thermal contraction cracks due to seasonal cooling defined polygons up to 35 m in size; this is an order of magnitude smaller than the largest crater floor polygons, suggesting another process for forming those polygons. El Maary et al. [2010] interpreted sediments in the craters as possible evidence of paleolakes, suggesting desiccation as an alternate or complementary process for formation of martian PPS.

El Marry et al. [2012] modeled the conditions of formation of large desiccation contraction polygons ranging 20-300 m in diameter on Earth and 80-350 m in diameter

on Mars. Their hydro-elastic model for desiccation was similar to the permafrost thermal contraction model of Mellon [1997], except in that it did not include the viscous creep that modulates thermal stresses. Temperature in Mellon's [1997] model was effectively replaced with water content, and the coefficient of thermal expansion with a shrinkage coefficient. El Marry et al. [2012] obtained polygon sizes that could exceed those arising from thermal contraction and reach the sizes of the largest polygons seen in crater floor deposits, offering support to a desiccation contraction formation process. This result provides additional impetus for examining low-latitude martian crater-fill PPS – such as Glenelg PPS – for evidence of formation by desiccation-induced contraction.

1.2. Study Site

On August 5, 2012, the Curiosity rover landed in Gale Crater, a low-latitude martian impact crater dating to 3.8-3.5 Ga [Anderson and Bell, 2010]. This study focuses on the deposits in Yellow Knife Bay, within the Glenelg region of Gale Crater 400 m east of the rover's landing site (4.6° S, 137.4° E) (Fig. 4). The study site is at the distal end of the Peace Vallis alluvial fan [Williams et al., 2013].

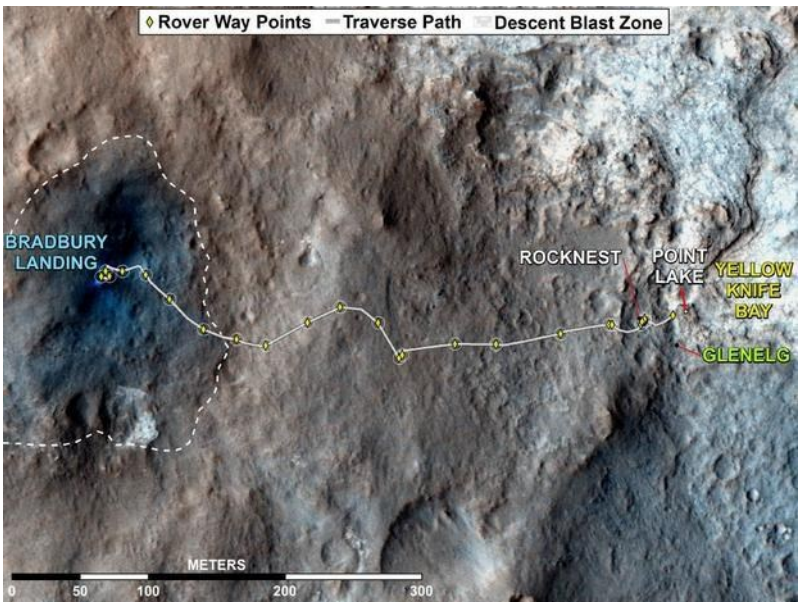

Figure 4. Curiosity rover's traverse from Bradbury Landing to the Glenelg region. The Peace Vallis alluvial fan extends to the north of this figure. Image credit: NASA/JPL-CalTech/Univ. of Arizona.

The rover photographed an extensive bedding plane broken up into slabs forming a distinct flagstone-like network at Glenelg. The network of parallel-sided, narrow linear gaps between flagstones is highly suggestive of contraction fractures (Fig. 5, planar-projected in Fig. 6).

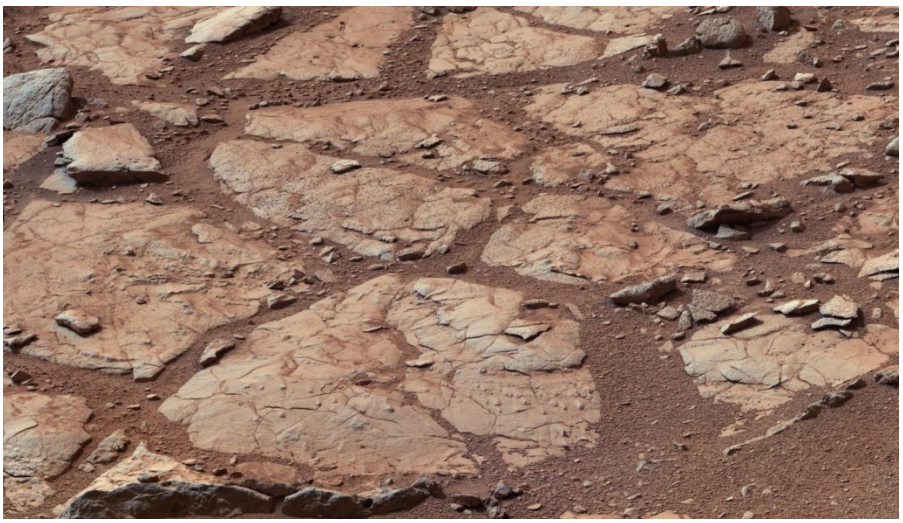

Figure 5. Sol 137 Mastcam 100mm image of PPS at Glenelg. Image frame bottom approximately 1 m wide. Photo: NASA/JPL-CALTECH/Caltech/MSSS.

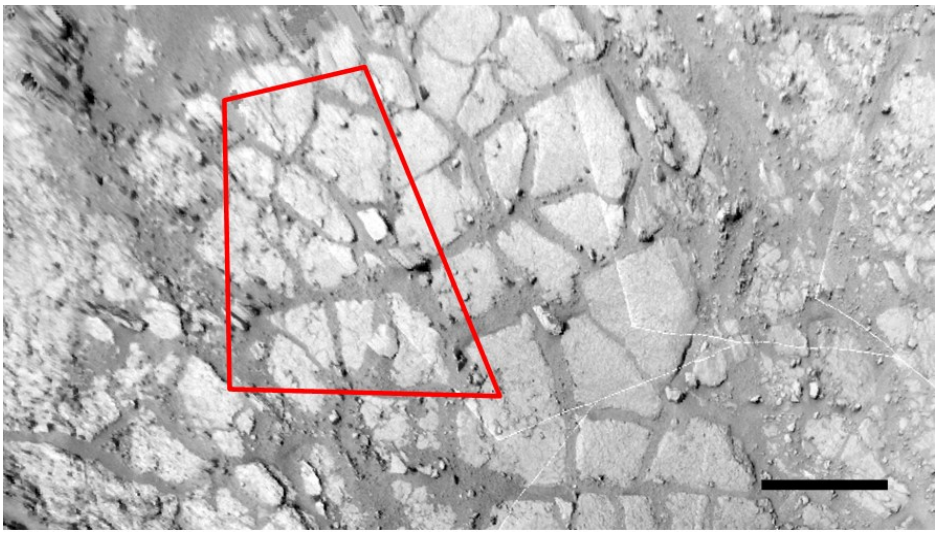

Figure 6. Planar projected sol 125 Navcam images, with approximate extent of Fig. 5 overlaid; Fig. 5 was taken looking toward the lower side of Fig. 6. Scale is indicated by 1 m-bar, lower right [Sletten, pers. com.].

The polygons of Glenelg PPS are an order of magnitude smaller than those of the PPS seen on HiRISE images in Gale Crater outside Glenelg, e.g., PPS located 0.5 km north of Glenelg. Those large polygons have not been photographed by Curiosity; their formative process is outside the scope of this thesis.

Glenelg was initially chosen as a study site by the Curiosity Science Team because the region exhibits high thermal inertia (resistance to temperature change) in Thermal Emission Imaging System (THEMIS) imagery. Fergason et al. [2006] interpreted the high thermal inertia as possible evidence of fine-grained sedimentary beds at Glenelg.

Prior to the rover's landing at Gale Crater, the MSL science team subdivided Glenelg terrain into several geological units, mapped on HiRISE imagery (Fig. 7).

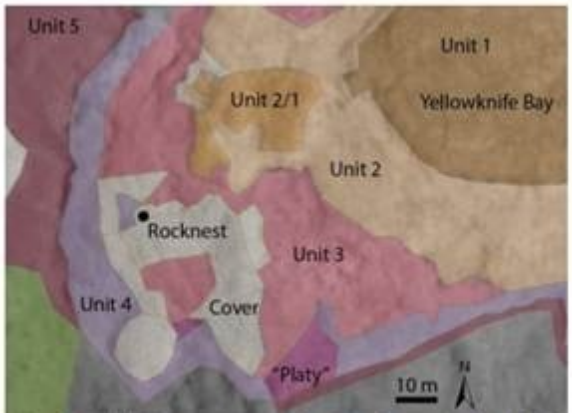

Figure 7. Geologic map of Glenelg region [Sumner et al., 2013].

Unit 1 was characterized as fractured, well-stratified bedrock. Unit 2, directly above unit 1, contained fewer fractures and decimeter-thick interbeds. However Curiosity's *in situ* imaging has modified that initial characterization. The PPS horizontal bedding planes in these two geological units look much alike in Curiosity images. Therefore in this study, unless otherwise noted, the two units are treated as a single undifferentiated unit, in which "Glenelg PPS" is developed.

2. Methods

Three quantitative methods will be used to characterize Glenelg PPS for evaluation of the playa desiccation hypothesis.

Directionality will be measured first. The Rayleigh Test [Zar, 2010] will determine whether the strike of PPS fractures deviate significantly from the random orientation expected of desiccation fractures in playa sediment or other contraction fractures in laterally uniform material. This test can distinguish contraction cracks from other cracks (tectonic and impact) that tend to have preferred orientations. It does not differentiate between mechanisms causing the contraction. Hotelling's Test [Zar, 2010] will be used to determine whether the widths of fractures exhibit significant directionality, as possible evidence of widening by aeolian scour, which would tend to have a preferred orientation aligned with the dominant wind direction.

Secondly, PPS fracture patterns will be characterized using Minkowski densities. These geometric and topological measures provide quantitative metrics of the patterns. One metric, the perimeter density, will be calculated as a possible indicator of desiccation PPS.

Thirdly, the magnitude of volumetric contraction reflected in the Glenelg PPS will be derived from the observed areal contraction, and compared to the contraction estimated for some terrestrial playa and other fine-grained sediments.

2.1. Directionality of Fractures

In a homogenous desiccating playa surface, the horizontal pre-fracture tensile stress is isotropic and the vertical stress vanishes at the surface. Accordingly, initial fractures are

near vertical and their strike is random. Fractures initiate at weak points that are assumed to be randomly distributed [Weinberger, 1999]. The strike of fractures would tend to be uniformly distributed.

The Rayleigh Test for uniformity indicates whether the observed fracture strike directions have the expected uniform distribution, by determining whether the null hypothesis of uniform distribution can be rejected. The test value, z, equals the number of measurements times the mean vector, or first trigonometric moment of the circular distribution [Batschelet, 1981]. If z is greater than the z-value for a normal distribution the null hypothesis is rejected. The Rayleigh Test for uniformity was calculated in the circular statistics software package Oriana 4.02 after Zar [2010].

2-D fracture patterns in Glenelg PPS can be quantified as a further check of consistency with volumetric contraction. However this quantification is meaningful only if the fracture patterns have remained essentially unaltered after formation. Aeolian scouring could widen fractures in the direction of the dominant wind, and exaggerate the apparent contraction of bordering polygons. Aeolian scouring appears to have altered Gale Crater rock surfaces and landforms [e.g., Thomson et al., 2011], where yardangs parallel the direction of Mt. Sharp slope winds theorized by Kite et al. [2012]. Also there is smaller-scale evidence of aeolian erosion along the Curiosity rover's traverse. At the Hottah site (Fig. 8), for example, cm-scale clasts are supported by finer-grained matrix with common orientation [Hallet, pers. com.], suggestive of a wind shadow protected from aeolian abrasion (removal of fine-grained, less resistant material). This process was inferred previously [Thomas et al., 2005] for "blueberry" clasts at Eagle Crater, Meridiani Planum.

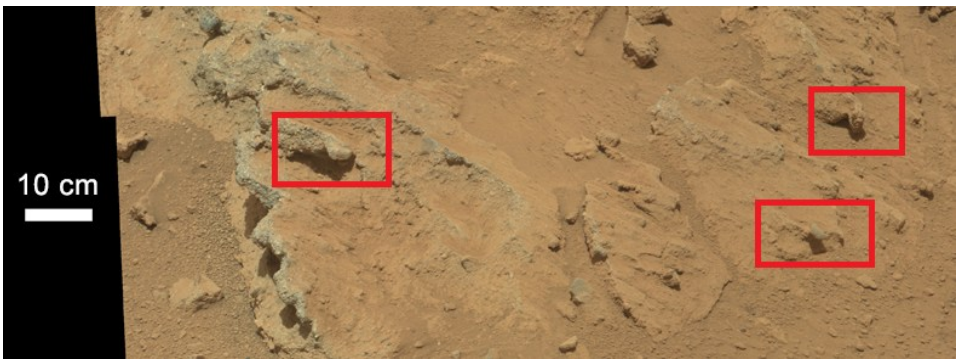

Figure 8. Evidence of aeolian erosion along Curiosity's traverse: cm-scale clasts (red boxes) are supported by finer-grained matrix with common orientation. Sol 39 Mastcam 100mm image, Hottah site, Gale Crater. Photo: NASA/JPL-Caltech/MSSS.

Glenelg sediments are likely to be susceptible to aeolian scouring because the bedding planes exposed at Glenelg have been exhumed, presumably by aeolian deflation, and the exposed bedding surfaces are so soft that they were easily scratched with the wire brush of Curiosity's Dust Removal Tool [NASA, JPL-Caltech, MSSS, 2013], (Fig. 9), and drilled by the Powder Acquisition Drill System (PADS) [NASA, JPL-Caltech, 2013].

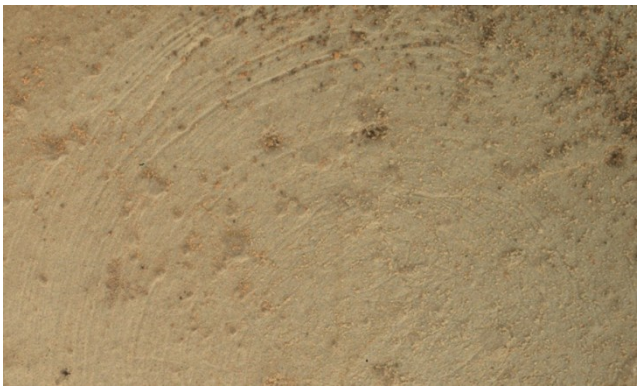

Figure 9. Brush scratches are visible. Sol 173 Mars Hand Lens Imager (Mahli) image of Wernecke brush target, John Klein, Glenelg, Gale Crater. Photo: NASA/JPL-Caltech/MSSS.

Glenelg imagery was examined to determine whether a directional widening is evident in the PPS fractures. Navcam images were planar-projected in ArcMap [Sletten, pers.

com.] for measurement of the fractures. Width and orientation of 97 large Glenelg PPS fractures were measured (Figs. 10, 11). These fractures were selected for maximum width, visual clarity, and geometric simplicity, and for minimal sediment cover.

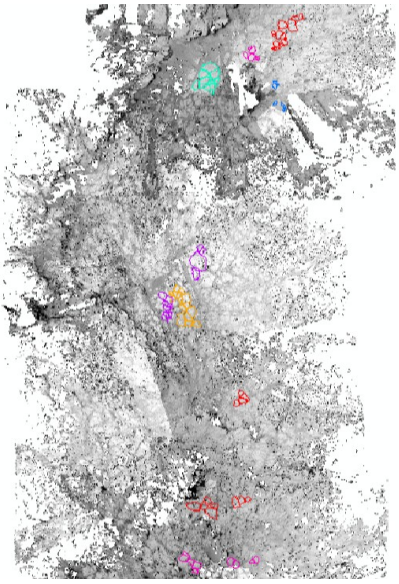

Figure 10. Polygons delineated by 97 measured fractures in Glenelg PPS. Photo: NASA/JPL-CALTECH/Caltech/MSSS [Sletten, pers. com.].

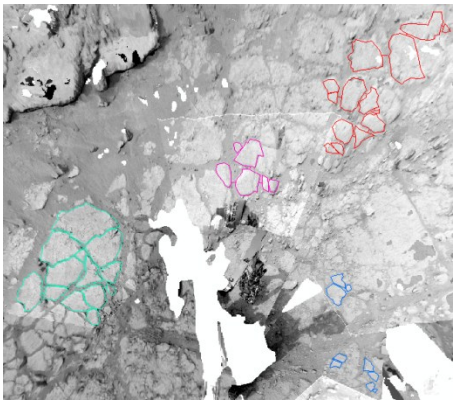

Figure 11. Subset of selected Glenelg polygons and fractures from Fig. 10. Photo: NASA/JPL-CALTECH/Caltech/MSSS [Sletten, pers. com.].

Imagery was georeferenced in EsriArcMap 10.1. Fracture width and axial orientation were measured in ArcMap with GIS-Media PetroGIS 1.5. Data were exported from

ArcMap with Data East XTools Pro 9.1.956. The fracture datafile was prepared in Microsoft Excel 2010. Plots and circular statistics were produced in Kovach Computing Services Oriana 4.02.

Data for fracture orientation and width were analyzed as circular data, in which each fracture's strike direction and width pair comprises a vector. All vectors in the dataset are weighted, and Hotelling's Test was applied to the weighted mean vectors [Batschelet, 1981]. Zar [2010] provides the version of Hotelling's Test used in Oriana 4.02. Hotelling's Test determines whether the centroid of the end points of the weighted vectors differs from the origin; i.e., whether the weighted angles have a significant mean direction. The test result is compared to the critical value corresponding with a null hypothesis: i.e., that there is no mean direction, hence no preferential widening of fractures in any direction. This hypothesis was quantified with a chosen significance level of 0.05, for the 97 measurements.

2.2. Fracture Patterns and Morphology

If an analysis of 2-D fracture patterns is to be useful for the present study, it must distinguish desiccation contraction patterns from patterns formed by other types of contraction, with at least one characteristic quantitative measure. Several approaches to the problem are possible.

The geometry of PPG is commonly quantified in terms of polygon size, number of sides and trough intersection angles [e.g., Kerfoot, 1972; Sletten et al., 2003]. However none of these measures distinguishes PPG from desiccation PPS, as desiccation of sediment can produce the same geometric characteristics as cooling of permafrost [Goehring, 2012]. Fractal dimension, a measure of complexity, has been used to

characterize real and simulated desiccation PPS fracture patterns [Valette et al. 2008], but the range of the dimensions was too broad to be diagnostic.

Another way to quantify fracture patterns is through spatial point pattern analysis (SPPA). SPPA was first applied to martian PPS by Rossbacher [1986], who calculated a nearest neighbor statistic for the mean of observed distances between polygon vertices and intersections. Comparison against the statistic for a random distribution classified the fracture pattern as clustered, random or regular. Rossbacher speculated that the technique could compare patterns produced by permafrost thermal contraction and desiccation. However SPPA studies have yet to explicitly compare and differentiate the patterns arising from each process [e.g. Haltigin et al., 2010].

Ulrich et al. [2011] quantified martian PPS through Principal Component Analysis (PCA), which determined relationships between polygon size and other dimensional variables. However, they considered only permafrost PPG, and within the range of PPG types, PCA had limited ability to distinguish between ice-wedge, sand-wedge, and sublimation polygons. Desiccation patterns were not analyzed.

These techniques have not therefore provided a quantitative measure to distinguish thermal contraction fracture patterns from desiccation fracture patterns. Vogel et al. [2005] explored a different approach to the problem, one that might distinguish the two processes. They calculated "Minkowski densities," observing that desiccation fracture patterns in sand-bentonite mixtures exhibited nearly identical values for "perimeter density" or "length density," over sand:bentonite ratios ranging from 5:1 to 1:1. This raised the possibility that perimeter density might be invariant for bentonite under desiccation, and by inference might be a quantitative measure that

could distinguish at least some desiccation fracture patterns from thermal contraction fracture patterns. To pursue that possibility in this study, Glenelg PPS fracture patterns were characterized by Minkowski densities, and the results were compared to those for terrestrial examples of thermal contraction in permafrost and desiccation contraction in expansive sediments. Minkowski densities did not, however, prove to be diagnostic of the mechanism causing contraction, contrary to the speculation of Vogel et al [2005]; the technique and results are summarized in Appendix 4.

2.3. Magnitude of Sediment Contraction

If Glenelg PPS is the product of playa desiccation, the volume-moisture characteristics, grain size and mineralogy of the sediments that formed the Glenelg bedrock should be similar to those of sediments of at least some known terrestrial playas.

First, Glenelg PPS would be expected to exhibit contraction upon drying with magnitude similar to known playa sediments. Glenelg PPS imagery was compared to images of desiccated fine-grained sediments from playas or similar settings. Areal contraction, $(\Delta L/L)^2$, was estimated from mean fracture width (aperture), taken from linear transects on images of mud cracks, and mean polygon length scale, taken to be the mean square root of the areas of polygons bordering the fractures. Fractures and polygons were measured in ArcMap 10.1.

Next the areal contraction of Glenelg polygons was calculated more precisely, to provide a more robust comparison of Glenelg PPS and playa desiccation contraction. It was assumed that prior to fracture formation, the polygons initially formed a continuous sediment layer. To obtain the best measure the areal contraction of Glenelg PPS, the areas of both the polygonal flagstones and intervening gaps, assumed to be fractures, in

the projected Navcam imagery were measured. The polygons were treated like jigsaw pieces and assembled into the smallest area that could contain the contracted material. This removed the total gap area, which is effectively the areal contraction.

To measure the contraction, individual polygons were translated and rotated in Photoshop 13.0.1 to piece them into a nearly continuous reconstruction of the total area of contracted polygons. Assuming isotropy of sediment contraction, the areal contraction corresponds to a volumetric contraction of $(\Delta L/L)^3$. However, measures of areal contraction cannot be readily compared to volumetric contraction because the contraction may be highly anisotropic. Kitsunezaki [2009] measured the thickness in drying calcium carbonate paste, recording a vertical contraction of 43% prior to the initiation of contraction cracks and horizontal contraction. This vertical contraction greatly exceeded the final horizontal contraction. Therefore an isotropic volumetric contraction provides a lower limit on the actual volumetric contraction.

The lower limit of volumetric contraction of Glenelg PPS and estimated volumetric contraction of expansive sediments in terrestrial playas were compared to one another; for the latter, published data were used. Neal et al. [1968] reported several measurements of grain size distributions and Atterberg limits for sediments from playa sites featuring desiccation fractures in the Basin and Range Province of North America. These measurements were used to estimate the volumetric contraction in playa sediment, down to the "shrinkage limit," the solid state below which no further contraction is detectable [Bell, 2004].

Volumetric contraction is the opposite of the widely used "swelling potential" (SP) [e.g., Murthy, 2002], which is a percentage change in volume from increased

moisture content, or degree of swelling [Rao et al., 2011]. It is determined experimentally with an oedometer [e.g. Murthy, 2002], wherein a laterally confined sample is soaked; or else it is measured with soil suction [e.g., Rao et al., 2011]. High SP is correlated with high fine-particle "clay" (<2 μm) fraction [Holtz and Kovacs, 1981]. Typically these are fractions of highly-expansive smectites or the less-expansive illites [Lambe and Whitman, 1979]. However no single factor can completely account for the SP. As Holtz and Kovacs [1981] state:

> "…swelling depends on the clay minerals present in the soil, the soil structure and fabric and several physico-chemical aspects of the soil such as cation valance, salt concentration, cementation and presence of organic matter."

For the purpose of this study, "sediment" will be used instead of "soil," to reflect the hypothesized deposition of the observed Glenelg rock without significant pedogenic activity, and "clay" will mean "<2 μm particle-size fraction," rather than clay mineral. Where clay minerals are indicated, they will be named.

Many empirical relationships have been proposed for estimating SP [Rao et al., 2011]. The equation of Muntohar [2006] is attractive because of the large number of soil samples analyzed (81), and the formal multiple linear regression analysis that was used to determine the variables that are significant predictors of the SP value. It has the form:

$$SP\ (\%) = 0.171\ CF + 0.0012\ LL + 0.409\ PI - 1.869 \quad (1)$$

where CF represents the clay fraction (% wt of material <2 μm), LL, the liquid limit (water content at which soil changes from plastic to liquid behavior) and PI, the

plasticity index (range of water contents over which the soil exhibits plastic behavior). Neal et al. [1968] provide the CF, LL and PI data required for calculation of playa sediment SP by equation (1).

3. Results

The directionality of fractures and fracture widths, and the magnitude of contraction provide valuable information regarding the formation process of the Glenelg PPS.

3.1. Directionality of Fractures

To test for a uniform distribution of fracture orientations that would be consistent with random fracturing during contraction of a uniform, horizontal sediment layer, the Rayleigh Test for uniformity was performed [Zar, 2010] using Oriana 4.02. Fracture strike orientations are plotted in Fig. 12, and tabulated in Appendix 1.

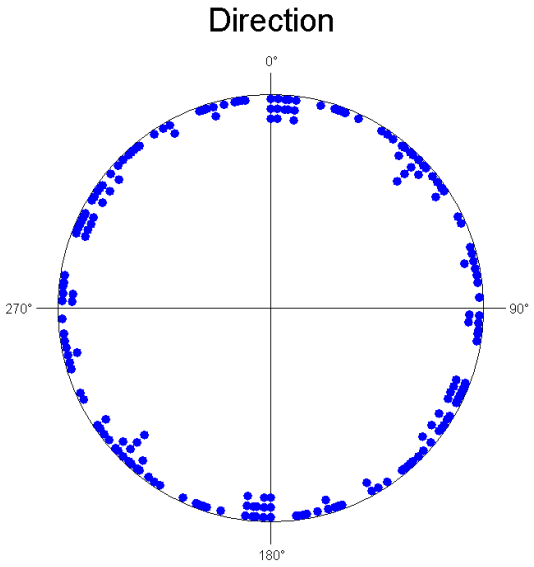

Figure 12. Fracture strike orientation (0-180°) for 97 Glenelg PPS fractures. 0° is North. Axial orientations are copied +180° to emphasize bidirectionality.

A significance level of 0.05 was chosen for the test of 97 measurements, giving a test value z (0.05)97 of about 2.988 [Zar, 2010]. The z-value for the fracture orientations was 0.223, considerably less than 2.988, hence the null hypothesis of uniform

distribution was not rejected, which is consistent with the fractures being contraction cracks.

To look for evidence of aeolian scour or for other processes that would tend to preferentially widen crack openings in directions of dominant aeolian sediment transport and thereby give rise to preferred directions, Hotelling's Test [Zar, 2010] was applied to the 97 fractures using Oriana 4.02, to determine whether the width-weighted axial orientations have a significant mean direction. Axial orientations and widths of the fractures are plotted in Fig. 13.

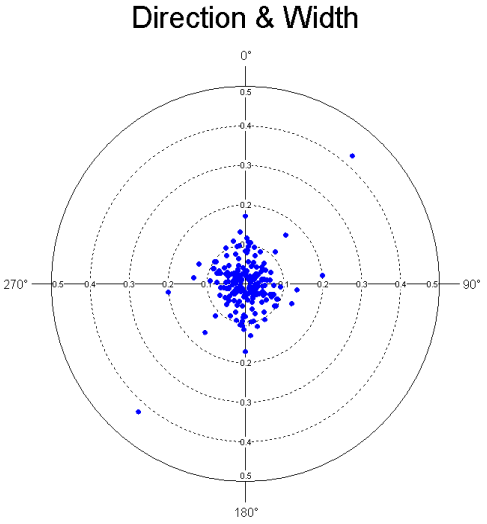

Figure 13. Fracture strike orientation (0-180°) and width (in m, shown as radial distance from plot center) for 97 Glenelg PPS fractures. 0° is North. Axial orientations are copied +180° to emphasize bidirectionality.

The null hypothesis was that of no mean direction, or no widening of fractures along a preferred direction. This hypothesis was quantified with a chosen significance level of 0.05 for the 97 measurements. The Hotelling's Test critical value, $F(0.05)_{2,95} = 3.09$, is the null distribution for the significance level (0.05) and degrees of freedom given as 2 and 97-2 =95 [Zar, 2010]. For the measured Glenelg fractures, F = 0.582, considerably

less than 3.09, and hence the null hypothesis (no significant mean direction) was not rejected. Aeolian scour under a dominant wind direction or other processes, such as tectonics or impacts, that would tend to produce fractures with preferred orientations are not evident in the exposed Glenelg bedding planes.

3.2. Fracture Intersection Angles

In addition to Minkowski densities (Appendix 4), another measurement used by Vogel et al. [2005] merits discussion. They measured angles of fracture bifurcation at regular time intervals during a single desiccation event, noting a common shift in the frequency distribution of angles, which evolved from 120° to 90° as fracture branchings evolved into a coalescence of existing fractures. A similar evolution in intersection angles of fracture is also seen to emerge after repeated contraction-expansion cycles. Sletten et al. [2003] reported thermal contraction fractures in Antarctica with dominant intersection angles near 90° in the PPS of Victoria Valley, and closer to 120° in the PPG of Beacon Valley. They interpreted this difference as reflecting different stages in PPG development, with intersections evolving from 90° to 120° as recurrent cycles of thermal forcing regularized the polygons. Interestingly, Goehring [2012] also observed a maturation of desiccation fracture angles, in this case advancing from 90° to 120°, in mud slurry undergoing several cycles of wetting and drying. Thus fracture angles for thermal contraction PPG and desiccation contraction PPS overlap broadly, and do not indicate the formation process.

3.3. Magnitude of Sediment Contraction

The horizontal contraction of the sediments in Glenelg PPS was compared to contraction due to desiccation in diverse fine-grained terrestrial sediments, using linear transects on images of mud cracks. Mean fracture width and mean polygon length scale provide an estimate of the areal contraction, $(\Delta L/L)^2$. Mean fracture width gives only a rough estimate of horizontal fracture area, resulting in an estimate of areal contraction with error up to 25%. Images of the examined mudcracks are included in Fig. 14, and corresponding estimates of areal contraction are shown in parentheses as follows: (a) Glenelg PPS (21% +/- 5%), (b) clinoptilolite-rich sediments (36% +/- 9%), (c) zeolite-rich sediments (12% +/- 3%), (d) interdune sediments with 0.1 m-scale PPS (24% +/- 6%), and (e) calcium carbonate paste (5% +/- 1%) with grain size averaging 1.5 μm [Kitsunezaki 2009; 2011].

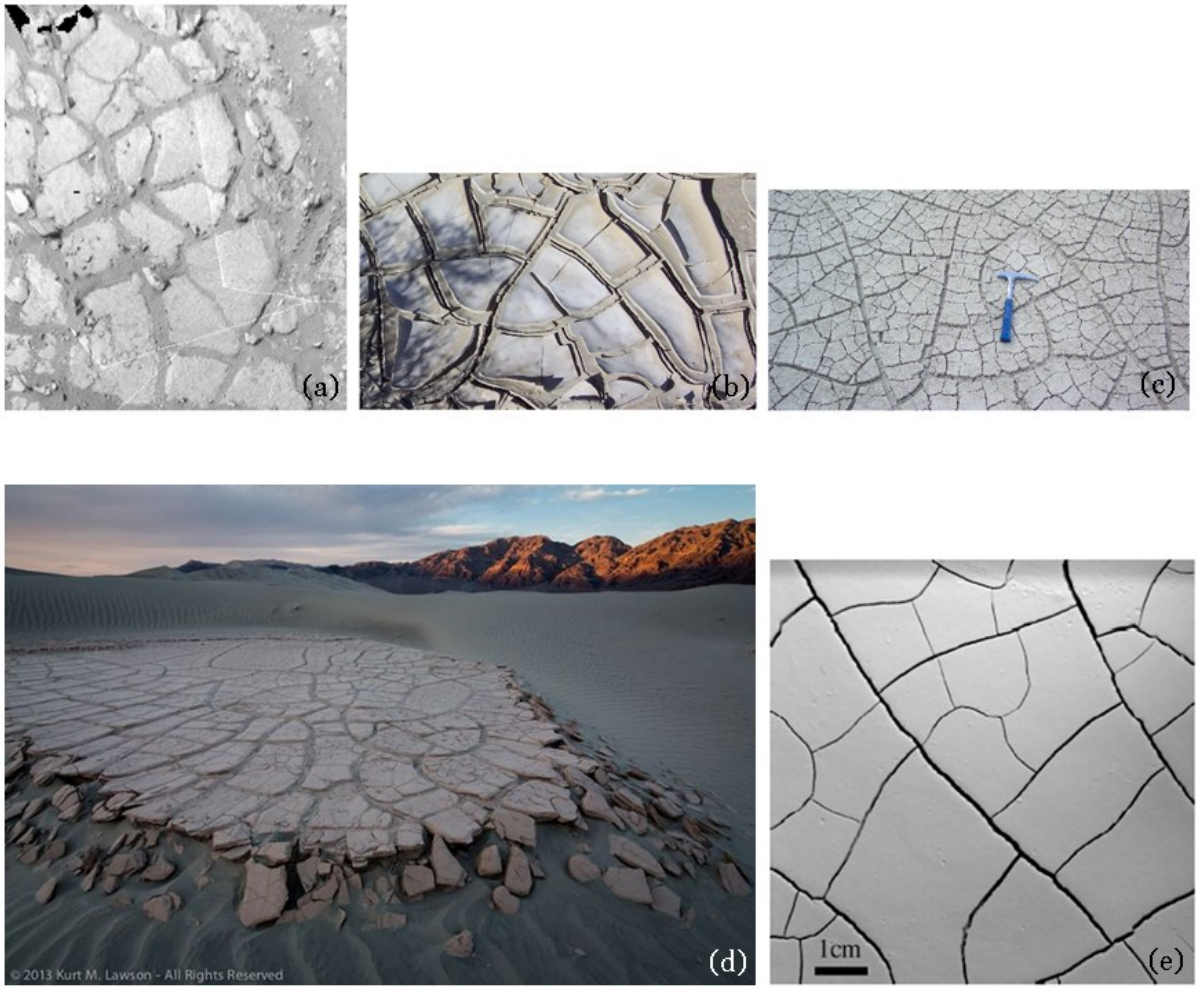

Figure 14. (a) Sol 125 Glenelg PPS planar projection. Photo: NASA/JPL-CALTECH/Caltech/MSSS. (b) Clinoptilolite-rich zeolite tuff, Lake Tecopa, south of Shoshone, CA. Photo: D. Bish. (c) Zeolite-rich mud puddle, Billie Mine, Dante's View Road, Death Valley National Park, CA. Photo: D. Bish. (d) Exposed plates of desiccated interdune sediment in Last Chance Range, Death Valley National Park, CA. Unknown mineralogy, exposure approx. 3 m across. Photo: Kurt M. Lawson. (e) Paste of calcium carbonate, no smectite [Kitsunezaki, 2011].

In the examples of Fig. 14 Glenelg PPS exhibits contraction within the range of sediment contraction common to playas, and considerably more than that of pure calcium carbonate.

To obtain a robust measure of the areal, horizontal contraction of a Glenelg PPS site, planar-projected imagery with a large number of clearly defined polygons was selected. The planar-projected imagery is presented alongside the contracted polygons

in Fig. 15.

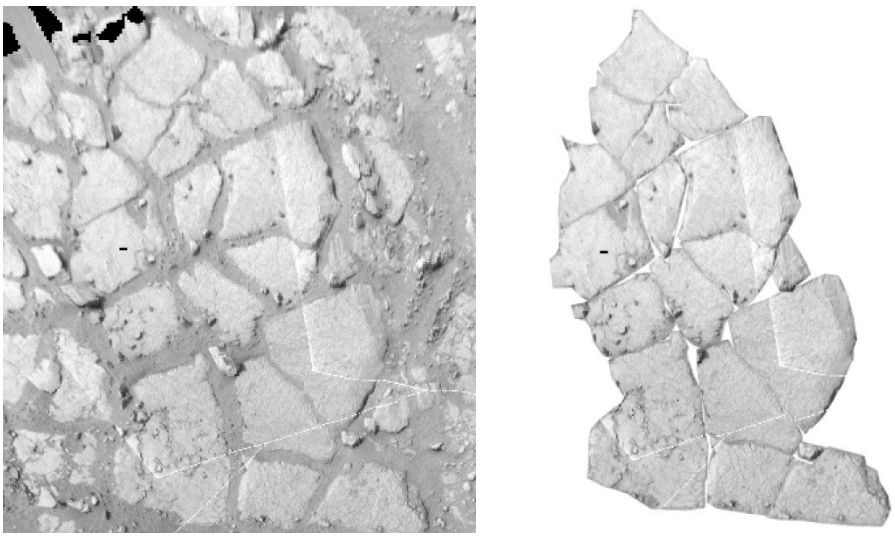

Figure 15. (left) Sol 125 Glenelg PPS planar projection and (right) contraction area reconstruction. Photo: NASA/JPL-CALTECH/Caltech/MSSS [Sletten, pers. com.].

In Fig. 15 the areal contraction (area of the gaps between flagstones divided by the total area) is 17.1%. The polygons fit closely, with a misfit area (residual gaps due to non-parallel polygon faces) of 3.2%. This misfit is conservatively assumed to be obscured, eroded or dislocated polygon material, and not additional contraction beyond the 17.1% calculated. Taking into account the 3.2% area misfit, the areal contraction ranges from about 14 to 20%. The estimate of areal contraction reported above, derived from mean fracture width and mean polygon length scale, is comparable but slightly higher, 21%. The volumetric contraction corresponding with the measured areal contraction of 17.1% is 24.5%. In all likelihood, however, the volumetric contraction exceeded this value because vertical contraction is likely much larger than the horizontal contraction, as it is unimpeded in the initial portion of the drying phase before contraction cracks form, when little if any horizontal contraction occurs [e.g., Kitsunezaki 2009; 2011].

4. Discussion

Results are interpreted in the broad geological context of Gale Crater, utilizing terrestrial playa analog sites. The measured Glenelg PPS volumetric contraction is compared to contraction of sediments in a terrestrial playa. Alternate formation hypotheses are also considered.

Contraction crack formation in both cooling permafrost and drying sediments requires water to provide either the icy cohesion that can transmit stresses over distances much larger than the grain size or to cause the volumetric contraction. This requirement adds independent support to the growing body of evidence for the former presence of water in the Glenelg region, and contributes to the growing consensus that water has flowed in Gale Crater. Bradbury Rise, the Curiosity rover's landing site near the distal end of the Peace Vallis fan, is at an elevation of -4,400 m. The rover confirmed prior water flow in Gale Crater by imaging streambed pebbles up to 4 cm diameter on the fan. This size precludes aeolian transport, and grain size distribution is interpreted by Williams et al. [2013] as evidence of fluvial flow with velocity of 0.20 to 0.75 m/s. Also Palucis et al. [2013] interpret the fan's gravel, low slope, inverted channels, and lack of lobate deposits as evidence of fluvial flow.

Streambed imagery supports previous studies of remote sensing data suggestive of water flow in Gale Crater [Anderson and Bell, 2010]. Extensive fluvial flow into a closed basin would produce lakes, and indeed, a series of lake levels have been inferred with four distinct levels preserved as benches and deltas [Dietrich et al., 2013]. The lowest level was a cluster of closed depressions at the toe of the Peace Vallis fan, which

they interpreted as a possible site of episodic shallow lakes. The Glenelg region is one of these depressions, adjacent to and east of the Bradbury Rise (Fig. 16).

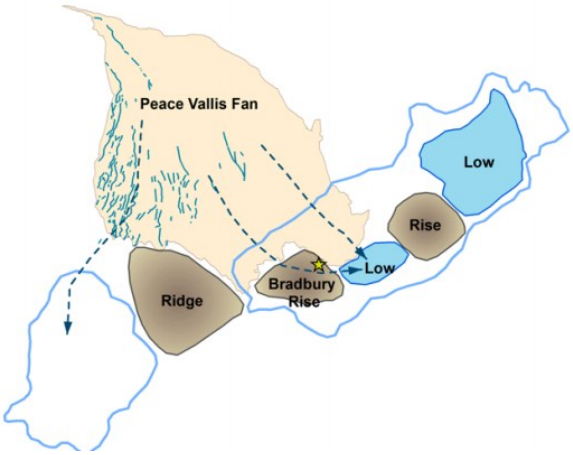

Figure 16. Glenelg region is the "Low" adjacent to and east of Bradbury Rise. Arrows mark inferred water flow direction. Blue outlines mark hypothetical former lake levels [Palucis et al., 2013].

Sediments would have been well sorted in the lake, with the size of sediment particles being inversely related to the water's turbulent energy, which is very low at deep distal sites [Abrahams and Parsons, 1994] such as is suggested for Glenelg, where finer particles would tend to accumulate [Hardie et al., 1978]. Desiccation cracks would be most likely to form at such sites where fine-grained sediments exposed in a mudflat or playa would contract upon drying.

Are Curiosity observations and study results consistent with this hypothesis? The comparison of the volume-moisture characteristics of the Glenelg sediments and of fine-grained sediments in which contraction cracks formed in known settings on Earth is particularly instructive. The areal contraction of polygons of the Glenelg PPS fractures were measured, providing a basis for comparison with terrestrial data on volumetric

contraction and the corresponding swelling potential (SP) of sediments. For the terrestrial playas studied by Neal et al. [1968], SP values can be estimated based on grain size and standard geotechnical properties, the Atterberg limits, using equation (1) (Table 1).

Table 1. Fine-grained particle (< 5 5 μm) content and Atterberg limits for sediments from fractured playas [Neal et al. 1968], and corresponding swelling potential calculated using equation (1), following Muntohar [2006].

Playa	% Particle Size < 5 μm	Plasticity Index (PI)	Liquid Limit (LL)	Swelling Potential (SP) %
Red Lake	55	21	42	16.2
Indian Springs	30	12	27	8.2
Ivanpah	56	20	41	15.9
Bicycle	45	14	36	11.6
North Paramint	32	14	37	9.4
Rosamond	71	30	52	22.6
Rogers	65	23	46	18.7
Coyote	53	24	46	17.1
Animas	65	6	27	11.7
Alvord	35	14	46	9.9
Eldorado	49	22	42	15.6

The 24.5% volumetric contraction at Glenelg is slightly higher than the estimated SP of these North American playa sediments. The highest estimated SP, 22.6% at Rosamond Playa, is close to that of Glenelg PPS. However the particle-size fractions recorded for these playas do not match exactly to clay-size fraction of equation (1). The smallest playa particle-size fraction is < 5μm, which is larger than the Muntohar [2006] clay particle-size fraction, < 2 μm. Therefore Table 1 likely overstates the "clay fraction," and the SP of the playa sediments.

The following abundance of clay minerals in Rosamond Playa samples is reported by Neal et al. [1968] using the qualitative scale of 1 (most abundant) to 5 (least): illite (1), chlorite-vermiculite (1-2), montmorillonite (3), and kaolinite (none-trace). The presence of illite and montmorillonite is consistent with the expansive nature of the playa sediments and desiccation fractures at Rosamond Playa.

These data on the mineralogy and grain size of terrestrial playas provide an interesting comparison with the John Klein sample. NASA et al. [2013b] and NASA and JPL-Caltech [2013] report that the John Klein sample contains ~20 wt% smectite fraction. The montmorillonite fraction at Rosamond Playa is poorly constrained (3 on a scale of 1-5), but also appreciable. The fraction of particles <5 μm diameter at Rosamond Playa is reported by Neal et al. [1968] at 71%. Images of the brushed and drilled rocks at John Klein do not resolve grains in the Mahli images, indicating that the particles at John Klein are smaller than ~40 μm in diameter, which is a small multiple of the finest resolution, about 14 μm, attainable with Curiosity's Mahli camera [Edgett et al., 2009]. Because of their fine-grained nature and mineralogy, the sediments that form the mudstone at Glenelg are also expected to be expansive. The similarities between Glenelg and Rosemond Playa in the magnitude of contraction, smectite mineralogy, and fine-grained fraction of the sediments collectively suggest that Rosamond Playa PPS is an excellent candidate analog for Glenelg PPS.

4.1. Alternate Hypotheses

The magnitude of contraction of Glenelg PPS is consistent with desiccation of expansive sediments; however other mechanisms could form similar PPS. Three potential

candidates are considered: thermal contraction, seismite formation, and subsurface collapse.

Rapid cooling of permafrost can produce deep contraction cracks, along which a wide trough between elevated borders can form due to recurrent thermal cycling and incremental filling of the crack [Lachenbruch, 1962; Sletten et al., 2003]. The separation between 0.3 to 1 m-wide mudstone slabs/flagstones at Glenelg averages 6.4 cm, and slabs show little or no visual evidence of deformation due to repeated infilling events, suggesting that the fractures occurred in one, or a very limited number of events. The large shrinkage from a single event is better explained by drying sediments.

The largest permafrost fractures due to thermal contraction occur in ice-rich material that is cooled quickly for a prolonged period because the coefficient of thermal expansion of ice is five times greater than that of silicates [Greene, 1966]. The magnitude of the strain equals $\alpha\,\Theta$, where α is the linear coefficient of thermal expansion of ice and Θ is the magnitude of the cooling [Lachenbruch, 1962]. Given a representative value of $\alpha = 5 \times 10^{-5}$ / °K for ice-rich permafrost, cooling a 1 m block of permafrost by $\Theta = 100°$ K produces a contraction of 5 mm, and would open bounding fractures at the sides of such a block by the same amount. This is an order of magnitude smaller than the observed mean flagstone spacing at Glenelg, making the observed large spacing inconsistent with thermal contraction without extensive introduction of external material.

Increasing the permafrost's tensile strength would increase the possible strain. Extreme cold increases the tensile strength of ice, which doubles over a temperature drop of 71° K [Litwin et al., 2012]. At Gale Crater, the temperature range is 183° K -

273° K, sufficient only for a doubling of tensile strength and strain, which would still be inconsistent with the observed large fracture widths.

Thermal contraction fractures in permafrost delineate polygonal domains that are considerably larger than those making up the Glenelg PPS; they range from 10-35 m in Antarctic Dry Valleys [Sletten et al., 2003], and 3-6 m in the northern plains of Mars [Mellon et al., 2008; Mellon et al., 2009a]. This spacing of fractures occurs because contraction is constrained horizontally, and strain relieves the horizontal tensile stress in the region adjacent to the subvertical fractures [Lachenbruch, 1962]. At a horizontal distance of a few fracture depths the stress relief is negligible, and another fracture can form [Greene, 1966]. Extending his earlier analysis of thermal stresses in permafrost [Mellon, 1997], Mellon et al. [2008] used a finite element model to quantify this stress relief at the Phoenix landing site latitude (68.2° N) with a range of near-surface ice table depth (thickness of ice-free sediment above ice-cemented permafrost). In their model, mean temperature and rate of temperature change were key variables in the calculation of strain. For a northern plain polygon forming in permafrost with a shallow ice table (<6 cm) and with a diameter exceeding 10 m, the high rate of temperature change produced tensile stress within the polygon that grew to exceed the tensile strength of the interior, resulting in a new crack subdividing the polygon. The modeled permafrost stress was consistent with 5-m polygons, in accord with the observed diameter of contraction polygons in the northern plains of Mars: e.g., 4.6 m polygons at the Phoenix landing site [Mellon et al., 2009a].

Mellon's et al. [2008] model always produced PPG polygons greater than 2 m in diameter for all modeled martian permafrost ice table depths and thermal stress values.

This minimum diameter (2 m) is considerably greater than the diameter of the polygons of Glenelg PPS, which are 0.5 m scale.

Although thermal contraction is inconsistent with Glenelg PPS fracture widths or spacings between large bedrock slabs/flagstones at Glenelg, troughs formed by recurrent ice wedging or sand wedging could still grow to a width consistent with the observed spacing at Glenelg [Lachenbruch, 1962]. For example, on Earth in permafrost regions with abundant moisture, ice wedges are commonly two orders of magnitude wider than the opening of the thermal contraction fracture (Fig. 17).

Figure 17. Thermal contraction fracture in ice wedge about 4 m tall. Tuktoyaktuk, Northwest Territories, Canada [Osterkamp and Burn, 2003].

Such ice wedges form when the upper permafrost thaws and liberates water that drains into existing permafrost fractures below. This added water freezes, increasing the ice volume and ice wedge width. In cold, hyper-arid regions, thermal contraction fractures fill not with water but with wind-blown sand and finer-grained material, which ravel

into the fracture, producing sand wedges [e.g. Pewe, 1959]. In the current, hyper-arid permafrost conditions at Gale Crater, sand-wedges would be more likely than ice-wedges.

When permafrost warms it expands, producing compressive stress normal to the wedges. This stress and the longer term stress due to wedge growth deform the nearby permafrost by shouldering aside the edges of polygons, producing symmetric ridges and a widening trough (Fig. 18).

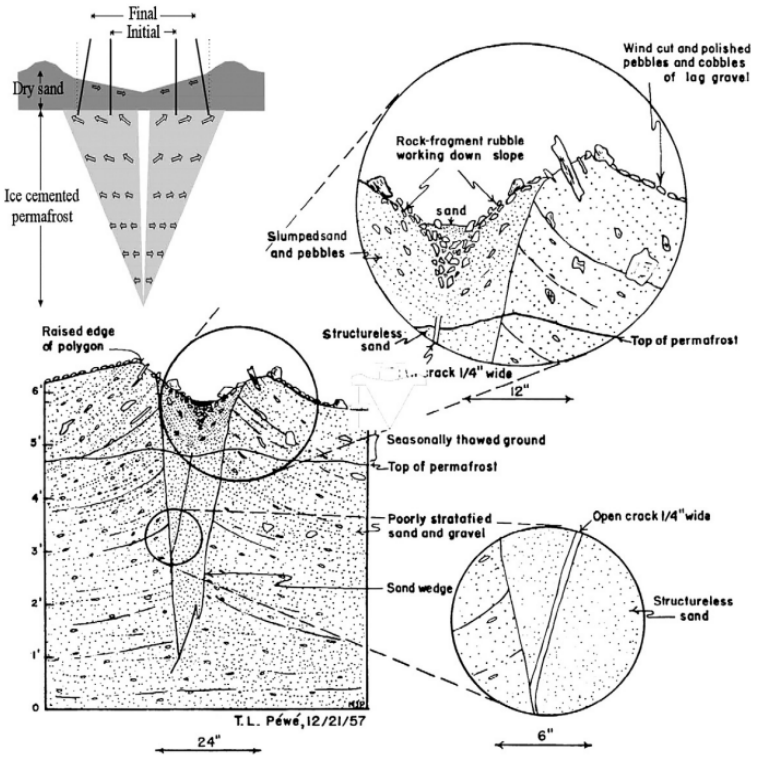

Figure 18. Deformation at the edges of two adjoining permafrost polygons due to growth of sand wedges. Note increasing upturn of layers toward surface [modified from Pewe 1959].

As one example, meter-wide sand wedges widen 0.51 to 0.64 mm per year in Victoria Land, Antarctica [Sletten et al., 2003] due to recurrent winter infill of sand. At this rate, it would take only about a century to form a sand wedge 6.4 cm wide – a geologically

rapid process. The relevance of this time scale to Glenelg PPG is unknown, however, because of the lack of information about the magnitude and frequency of crack opening and sand infilling at Glenelg. Moreover the Glenelg polygons are an order of magnitude smaller than the thermal contraction polygons of Antarctic Dry Valleys, resulting in correspondingly narrower fracture that would accumulate less fill and undergo slower trough growth.

Vertical growth of the wedges' symmetric ridges is slower than horizontal trough growth. The micro-relief developed in permafrost due to wedge growth in Antarctic Dry Valleys was modeled by Hallet et al. [2011]; their results included ridges that rise 0.24 m over 1500 years (Fig. 19).

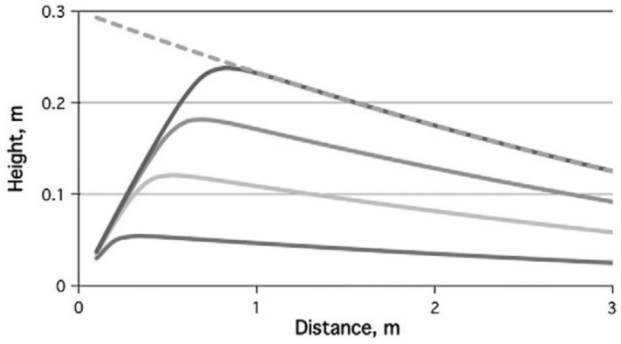

Figure 19. Computed surface relief caused by sand-wedge growth. Solid lines are sequential surface profiles starting from a level surface and rising with time. Dashed curve is profile without downslope raveling of sand [Hallet et al., 2011].

If wedge growth stops, erosion progressively lowers the ridges; they would vanish over the long term. However the deformation might still be visible in fully eroded ridges, provided that the host material is distinctly layered. Symmetric upturning of the sediments would be expected across troughs as shown in Fig. 19.

Lineations are evident in a few bedrock fragments and exposures at Glenelg, as in Figs. 20, 21; they suggest sedimentary layering that could record deformation associated with sand-wedge growth. However such deformation has not been recognized.

Figure 20. Sol 234 Mastcam 100mm photograph of faint lineations, John Klein site, Glenelg. Photo: NASA/JPL-CALTECH/Caltech/MSSS.

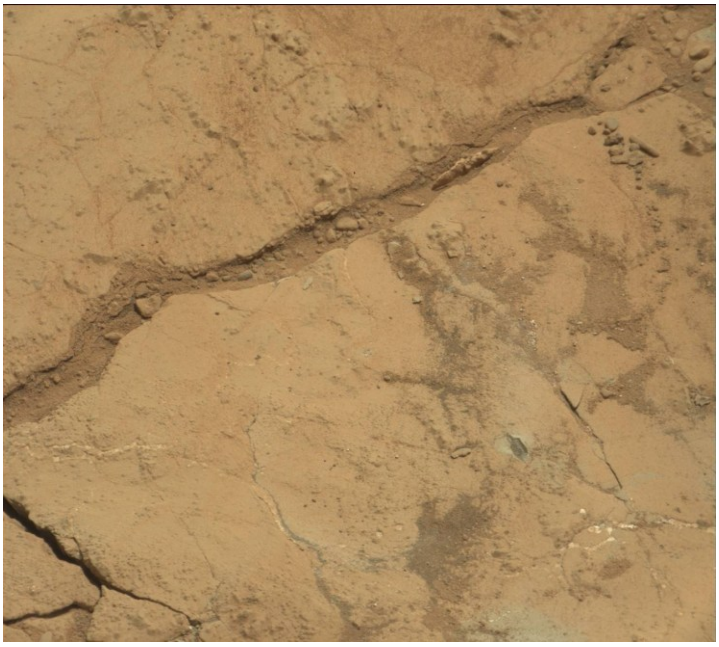

Figure 21. Sol 200 Mastcam 100mm photograph of faint lineations exposed at periphery of flagstone, John Klein site, Glenelg. Photo: NASA/JPL-CALTECH/Caltech/MSSS.

Notably, although stratigraphic exposures of the flagstones at Glenelg are very limited, there is no evidence of deformation of the bedding at the periphery of the flagstones in Glenelg imagery; hence former sand wedge-induced deformation is unlikely. Deep stratigraphic sections perpendicular to the polygon faces would be ideal to view this type deformation, but these do not exist.

Seismic disturbance is also known to produce polygonal networks with some similarity to the Glenelg PPS. Montenat et al. [2007] noted that the sediments most sensitive to seismic disturbance are those with alternating sand/silt beds and clay beds. Sedimentary rocks with texture ranging from clay to sand are visible at Glenelg, which raises the possibility that Glenelg sediments were sensitive to seismic disturbance at some time in the past.

Liquefaction of sediment during seismic disturbance produces diverse deformation features including sinusoidally folded veins with vertical axial planes [Pratt, 1998a], recumbent folds [Montenat et al., 2007], diapir-like intrusion structures [Montenat et al., 2007], sand volcanoes and extruded sand sheets [Maltmann, 1994]. In contrast, desiccation of fine-grained sediments produces vertically-tapered fractures, defining polygon interiors typically deformed only by curling in a thin surface layer of mud [Maltmann, 1994], which is rapidly eroded. The few exposures of the bedding at Glenelg do not suggest the pervasive deformation characteristic of seismically disturbed sediments (seismites), and the uniform orientation and alignment of the flagstones reflect essentially no deformation aside from the contraction fractures formed in a subhorizontal sediment layer.

Seismites in brittle material can form “pseudo mud cracks,” but the associated polygons are commonly tilted randomly due to spatially variable expulsion of sediment during the earthquake [Montenat et al., 2007] (Fig. 22).

Figure 22. Seismite in lacustrine limestone with injection dykes and random polygon tilts (block approx. 0.2 m long axis) [Montenat et al., 2007].

This random tilting contrasts with the planar alignment characteristic of desiccation PPG and Glenelg PPS.

Finally, the possibility of PPS formation by subsurface collapse is considered briefly. In Section 3.1 the Rayleigh Test for uniformity indicated that the PPS fracture orientations have a uniform distribution. This would be expected in desiccation PPS, but not in PPS formed from subsurface collapse of voids, where arcuate patterns of fractures form over the collapse due to relief of radially oriented stress. If voids were present and collapsing beneath Glenelg sediment at the time of PPS formation, arcuate fractures could have occurred, and Curiosity photographs covering a portion of the collapsing area would exhibit a preferred orientation of fractures. This is not seen in the Rayleigh Test results.

5. Conclusions

Polygonal patterned surfaces at Glenelg were studied to shed light on their formative mechanism. The most instructive measurements made were those of the magnitude of material contraction. The PPS at Glenelg suggest that prior to lithification, the mud at Glenelg contracted 24.5%, after vertical cracks formed. The best analog for this amount of contraction is desiccation of fine-grained sediment, based on known or estimated moisture-induced volumetric changes in sediments from fine-grained playas of the American Southwest (Table 1). An especially good correspondence with Glenelg PPS is seen in the magnitude of contraction and the similar flagstone network of the interdune sediments in the Last Chance Range (Fig. 14d).

Several other Curiosity observations and interpretations corroborate the inference of playa desiccation: 1) the fine texture of the John Klein sample (< 14 μm) is comparable to that of sediment (<20 μm) typical of mudflats and playas; 2) the subhorizontal polygon surfaces and uniform distribution of fracture orientations are similar to those in drying mudflats; 3) the 20% smectite mineralogy of the John Klein sample is similar to that commonly found in playa mudflats. Together the results suggest that Glenelg PPS is primarily the product of playa desiccation.

These results complement other findings that collectively document a past period of sustained fluvial flow in Gale Crater, and the formation of a lake above the current topographic depression of Glenelg. Fine-grained sediment (<20 μm) would have been deposited offshore, in the calm waters near Glenelg, away from active sediment sources [Hardie et al., 1978; Abrahams and Parsons, 1994]. Subsequent drying would have produced the mudflat and the contraction of the lacustrine sediments that resulted in

the observed PPS. Several geomorphic studies have reported evidence for paleolakes at Glenelg and the broader crater region, including shallow, transient lakes in Gale Crater [Irwin et al., 2005], a lake at Glenelg fed by sustained fluvial flow down the Peace Vallis fan [Williams et al., 2013; Palucis et al., 2013], and a succession of three descending deep lake levels in Gale Crater, terminated by a fourth level of shallow lakes inclusive of the Glenelg region [Dietrich et al., 2013]. Altogether this study corroborates the geomorphic studies by suggesting that Glenelg PPS is a record of a period in martian history when surface temperature and air pressure were sufficient for the ponding of liquid water.

References

Allen, G., Nabrzyski, J., Seidel, E., van Albada, G. D., Dongarra, J., & Sloot, P. (2009). Computational Science-ICCS 2009. Lecture Notes in Computer Science, 5545.

Anderson R. B. and Bell J. F. (2010). Geologic mapping and characterization of Gale Crater and implications for its potential as a Mars Science Laboratory landing site. Mars, 5, 76-128.

Batschelet, E. (1981) Circular statistics in biology. Academic Press, London. 372pp.

Bell, F. G. (2004). Engineering geology and construction. Taylor & Francis.

Black, R. F. (1976). Periglacial features indicative of permafrost: ice and soil wedges. Quaternary Research, 6(1), 3-26.

Das, B. M. (1983). Advanced soil mechanics.

Dietrich, W. E., Parker, T., Sumner, D. Y., Hayes, A. G., Palucis, M. C., Williams, R. M. E., ... & Team, M. S. L. (2013). Topographic Evidence for Lakes in Gale Crater. LPI Contributions, 1719, 1844.

Edgett, K., Ravine, M., Caplinger, M. A., Ghaemi, F. T., Schaffer, J. A., Malin, M. C., ... & Yingst, R. A. (2009). The Mars Science Laboratory (MSL) Mars hand lens imager (MAHLI) flight instrument (abstract# 1197). In 40th Lunar and Planetary Science Conference. CD-ROM.

El Maarry, M. R., Markiewicz, W. J., Mellon, M. T., Goetz, W., Dohm, J. M., & Pack, A. (2010). Crater floor polygons: Desiccation patterns of ancient lakes on Mars?. Journal of Geophysical Research, 115(E10), E10006.

El Maarry, M. R., Kodikara J., Wijessoriya S., Markiewicz, W. J., & Thomas N. (2012). Desiccation mechanism for formation of giant polygons on Earth and intermediate-sized polygons on Mars: Results from a pre-fracture model. Earth and Planetary Science Letters 323-324 19–26.

Fergason, R. L., Christensen, P. R., & Kieffer, H. H. (2006). High-resolution thermal inertia derived from the Thermal Emission Imaging System (THEMIS): Thermal model and applications. Journal of Geophysical Research: Planets (1991–2012), 111(E12).

Goehring, L. (2012). Evolving fracture patterns: columnar joints, mud cracks, and polygonal terrain. arXiv preprint arXiv:1211.6762.

Greene, G. W. (1966). Contraction theory of ice-wedge polygons: A qualitative discussion. In Permafrost international conference: proceedings 11-15 November 1963 Lafayette, Indiana (No. 1287, p. 63). National Academies.

Hallet, B., Sletten, R., & Whilden, K. (2011). Micro-relief development in polygonal patterned ground in the Dry Valleys of Antarctica. Quaternary Research, 75(2), 347-355.

Haltigin, T. (2010). Interpreting polygonal terrain network arrangements on Earth and Mars using spatial point patterns.

Hardie, L. A., Smoot, J. P., & Eugster, H. P. (1978). Saline lakes and their deposits: a sedimentological approach. In Modern and Ancient Lake Sediments: Proceedings of a Symposium Held at the HC Ørsted Institute, University of Copenhagen, 12-13 August 1977 (No. 2, p. 7). Halsted Press.

Holtz, R. D., & Kovacs, W. D. (1981). An introduction to geotechnical engineering (No. Monograph).
Howell, M. S., Buck, B., Rech, J. A., Brock, A., & Prellwitz, J. (2006, July). Genesis of the Hyperarid Soils of the Atacama Desert: Analogue for Mars?. In The 18th World Congress of Soil Science.
Irwin, R. P., Howard, A. D., Craddock, R. A., & Moore, J. M. (2005). An intense terminal epoch of widespread fluvial activity on early Mars: 2. Increased runoff and paleolake development. Journal of Geophysical Research: Planets (1991–2012), 110(E12).
Kerfoot, D. E. (1972). Thermal contraction cracks in an arctic tundra environment. Arctic, 142-150.
Kite, E. S., & Lewis, K. W. (2012). Growth and form of the mound in Gale Crater, Mars: Slope-wind enhanced erosion and transport. arXiv preprint arXiv:1205.6840.
Kitsunezaki, S. (2009). Crack Propagation Speed in the Drying Process of Paste. Journal of the Physical Society of Japan, 78, 6, 064801.
Kitsunezaki, S. (2011). Crack growth in drying paste. Advanced Powder Technology, 22, 311-318.
Kostama, V.-P., Kreslavsky, M.A., Head, J.W. (2006). Recent high-latitude icy mantle in the northern plains of Mars: Characteristics and ages of emplacement. Geophys. Res. Lett. 33 (L11201).
Kuzmin, R.O., Zabalueva, E.V. (2003). Polygonal terrains on Mars: Preliminary results of global mapping of their spatial distribution. In: Lunar and Planetary Science Conference XXXIV, Abstract #1912. League City, TX.
Lachenbruch, A. H. (1962). Mechanics of thermal contraction cracks and ice-wedge polygons in permafrost. Geological Society of America Special Papers, 70, 1-66.
Lambe T. W. and Whitman R. V. (1979). Soil Mechanics, SI Version, John Wiley & Sons.
Lammer, H., et al. (2013) Outgassing history and escape of the martian atmosphere and water inventory. Space Science Reviews 174.1-4: 113-154.
Legland, D., Kiêu, K., & Devaux, M. F. (2007). Computation of Minkowski measures on 2D and 3D binary images. Image Analysis & Stereology, *26*(2), 83-92.
Legland, D. (2011). "Geometric Measures in 2d-3d Images." Matlab Central.
Levy, J., Head, J., & Marchant, D. (2009). Thermal contraction crack polygons on Mars: Classification, distribution, and climate implications from HiRISE observations. Journal of Geophysical Research: Planets (1991–2012), 114(E1).
Levy, J. S., Marchant, D. R., & Head, J. W. (2010). Thermal contraction crack polygons on Mars: A synthesis from HiRISE, Phoenix, and terrestrial analog studies. Icarus, 206(1), 229-252.
Litwin, K. L., Zygielbaum, B. R., Polito, P. J., Sklar, L. S., & Collins, G. C. (2012). Influence of temperature, composition, and grain size on the tensile failure of water ice: Implications for erosion on Titan. Journal of Geophysical Research: Planets (1991–2012), 117(E8).
Malin, M.C., Edgett, K.S. (2001). Mars Global Surveyor Mars Orbiter Camera: Interplanetary cruise through primary mission. J. Geophys. Res. 106 (E10), 23429–23540.
Maltman, A. (Ed.) (1994). The Geological Deformation of Sediments. Chapman and Hall, London.

Mangold, N. (2005). High latitude patterned grounds on Mars: Classification, distribution and climatic control. Icarus, 174(2), 336-359.
Marchant, D. R., Lewis, A. R., Phillips, W. M., Moore, E. J., Souchez, R. A., Denton, G. H., ... & Landis, G. P. (2002). Formation of patterned ground and sublimation till over Miocene glacier ice in Beacon Valley, southern Victoria Land, Antarctica. Geological Society of America Bulletin, 114(6), 718-730.
Mellon, M.T. (1997). Small-scale polygonal features on Mars: Seasonal thermal contraction cracks in permafrost. J. Geophys. Res. 102 (E11), 25617–25628.
Mellon, M. T., Arvidson, R. E., Marlow, J. J., Phillips, R. J., & Asphaug, E. (2008). Periglacial landforms at the Phoenix landing site and the northern plains of Mars. Journal of Geophysical Research: Planets (1991–2012), 113(E3).
Mellon, M. T., Malin, M. C., Arvidson, R. E., Searls, M. L., Sizemore, H. G., Heet, T. L., ... & Marshall, J. (2009a). The periglacial landscape at the Phoenix landing site. Journal of Geophysical Research: Planets (1991–2012), 114(E1).
Mellon, M. T., Arvidson, R. E., Sizemore, H. G., Searls, M. L., Blaney, D. L., Cull, S., ... & Zent, A. P. (2009b). Ground ice at the Phoenix landing site: Stability state and origin. Journal of Geophysical Research, 114(E1), E00E07.
Michielsen, K., De Raedt, H., & De Hosson, J. T. M. (2003). Aspects of mathematical morphology. Advances in imaging and electron physics, 125, 119-194.
Montenat, C., & Barrier, P. (2007). Seismites: An attempt at critical analysis and classification. Sedimentary Geology, 196(1), 5-30.
Müller, G. (1998). Starch columns: Analog model for basalt columns. Journal of Geophysical Research: Solid Earth (1978–2012), 103(B7), 15239-15253.
Muntohar A. S. (2006). Prediction and classification of expansive clay soils. Expansive Soils. Ch. 3.
Murthy, V. N. S. (2002). Geotechnical engineering: principles and practices of soil mechanics and foundation engineering (Vol. 10). CRC Press.
Mutch, T. A., Arvidson, R. E., Binder, A. B., Guinness, E. A., & Morris, E. C. (1977). The geology of the Viking Lander 2 site. Journal of Geophysical Research, 82(28), 4452-4467.
NASA, JPL-Caltech (2013). NASA Curiosity Rover Collects First Martian Bedrock Sample. Press release. http://www.nasa.gov/mission_pages/msl/news/msl20130209.html
NASA, JPL-Caltech, MSSS (2013). Target 'Wernecke' After Brushing by Curiosity. Press release. http://www.nasa.gov/mission_pages/msl/multimedia/pia16790.html
Neal, J.T., Langer, A.M., Kerr, P.F. (1968). Giant desiccation polygons of Great Basin Playas. Geol. Soc. Am. Bull. 79, 69–90.
Ohser, J., & Mücklich, F. (2000). Statistical analysis of microstructures in materials science. New York: John Wiley.
Osterkamp T. E., Burn C. R. (2003). Permafrost. Encyclopedia of Atmospheric Sciences 1st ed. 1717-1729.
Palucis M. C., Dietrich W. E., Hayes A., Williams R. M. E., Calef F., Sumner D. Y., Gupta S., Hardgrove C., and the MSL Science Team (2013). Origin and Evolution of the Peace Vallis Fan System that Drains into the Curiosity Landing Area, Gale Crater. LPSC 1607.

Parsons, A. J., & Abrahams, A. D. (1994). Geomorphology of desert environments (pp. 3-12). Springer Netherlands.
Pechmann, J.C. (1980). The origin of polygonal troughs on the Northern Plains of Mars. Icarus 42, 185–210.
Pewe, T. L. (1959). Sand-wedge polygons (tesselations) in the McMurdo Sound region, Antarctica; a progress report. American Journal of Science, 257(8), 545-552.
Plummer, P. S., & Gostin, V. A. (1981). Shrinkage cracks: desiccation or synaeresis?. Journal of Sedimentary Research, 51(4).
Pratt, B. R. (1998a). Molar-tooth structure in Proterozoic carbonate rocks: Origin from synsedimentary earthquakes, and implications for the nature and evolution of basins and marine sediment. Geological Society of America Bulletin, 110(8), 1028-1045.
Rao B. H., Venkataramana K., Singh D. N. (2011). Studies on the determination of swelling properties of soils from suction measurements. Canadian Geotechnical Journal 48: 375-387.
Rossbacher, L. A. (1986). Nearest-neighbour analysis: a technique for quantitative evaluation of polygonal ground patterns. Geografiska Annaler. Series A. Physical Geography, 101-105.
Roth, K., Boike, J., & Vogel, H. J. (2005). Quantifying permafrost patterns using Minkowski densities. Permafrost and Periglacial Processes, 16(3), 277-290.
Seibert, N.M., Kargel, J.S. (2001). Small-scale martian polygonal terrain: Implications for liquid surface water. Geophys. Res. Lett. 28 (5), 899–902.
Sletten, R. S., Hallet, B., & Fletcher, R. C. (2003). Resurfacing time of terrestrial surfaces by the formation and maturation of polygonal patterned ground. Journal of Geophysical Research: Planets. 108(E4), 8044, doi:10.1029/2002JE001914.
Sumner, D. Y., Palucis, M., Dietrich, B., Calef, F., Stack, K. M., Ehlmann, B. L., ... & Williams, R. (2013). Preliminary Geological Map of the Peace Vallis Fan Integrated with In Situ Mosaics from the Curiosity Rover, Gale Crater, Mars. LPI Contributions, 1719, 1699.
Tang, C. S., Cui, Y. J., Shi, B., Tang, A. M., & Liu, C. (2011). Desiccation and cracking behaviour of clay layer from slurry state under wetting–drying cycles. Geoderma, 166(1), 111-118.
Thomas, M., Clarke, J. D. A., & Pain, C. F. (2005). Weathering, erosion and landscape processes on Mars identified from recent rover imagery, and possible Earth analogues. Australian Journal of Earth Sciences, 52(3), 365-378.
Thomson, B. J., Bridges, N. T., Milliken, R., Baldridge, A., Hook, S. J., Crowley, J. K., ... & Weitz, C. M. (2011). Constraints on the origin and evolution of the layered mound in Gale Crater, Mars using Mars Reconnaissance Orbiter data. Icarus, 214(2), 413-432.
Valette, G., Prévost, S., Lucas, L., & Léonard, J. (2008). A dynamic model of cracks development based on a 3D discrete shrinkage volume propagation. Computer Graphics Forum, 27(1), 47-62.
Vogel, H. J., Hoffmann, H., & Roth, K. (2005). Studies of crack dynamics in clay soil: I. Experimental methods, results, and morphological quantification. Geoderma, 125(3), 203-211.

Washburn, A. L. (1979). Geocryology—A survey of periglacial processes and environments. London, Edward Arnold, 402 pp.
Weinberger, R. (1999). Initiation and growth of cracks during desiccation of stratified muddy sediments. Journal of Structural Geology, 21(4), 379-386.
Weinberger, R. (2001). Evolution of polygonal patterns in stratified mud during desiccation: The role of flaw distribution and layer boundaries. Geological Society of America Bulletin, 113(1), 20-31.
Williams, R. M. E., Grotzinger, J. P., Dietrich, W. E., Gupta, S., Sumner, D. Y., Wiens, R. C., ... & Charpentier, A. (2013). Martian Fluvial Conglomerates at Gale Crater. Science, 340(6136), 1068-1072.
Zar, J. H. (2010). Biostatistical Analysis (5th edn) 944 pp.

Appendix 1 - Data for Directionality of Fractures

Axial orientation (0-180°) and width (m) for 97 measured fractures.

ID	Axial Orientation (0-180°)	Width (m)
1	94.09	0.049223
2	92.73	0.073731
3	2.12	0.079085
4	56.31	0.031661
5	151.26	0.103488
6	111.37	0.072293
7	40.36	0.424341
8	4.4	0.10539
9	151.19	0.040891
10	121.61	0.012561
11	122.47	0.054077
12	77.12	0.049635
13	141.34	0.034211
14	56.77	0.061745
15	126.43	0.092967
16	73.74	0.044523
17	83.83	0.198835
18	7.85	0.05706
19	42.06	0.070976
20	92.86	0.025735
21	160.02	0.049258
22	25.2	0.089449
23	99.46	0.033281
24	34.82	0.051098
25	47.12	0.037957
26	117.9	0.019108
27	171.03	0.028065
28	164.41	0.065136
29	112.78	0.129168
30	40.24	0.162243
31	146.31	0.085877
32	21.37	0.058826
33	164.22	0.112801

34	117.65	0.055942
35	48.01	0.031747
36	18.85	0.076182
37	2.39	0.084476
38	94.48	0.089954
39	173.83	0.13088
40	130.24	0.029944
41	125.42	0.097095
42	79.38	0.057249
43	51.95	0.051356
44	66.61	0.070883
45	97.11	0.043685
46	137.29	0.062219
47	167.47	0.09727
48	32.47	0.022927
49	172.57	0.040786
50	140.19	0.013734
51	133.15	0.038565
52	138.81	0.023494
53	0	0.081776
54	96.65	0.133509
55	124.51	0.042913
56	162.07	0.07898
57	126.87	0.066305
58	20.85	0.049667
59	115.46	0.089549
60	149.04	0.03723
61	45	0.012642
62	45	0.016629
63	87.4	0.032369
64	122.47	0.019164
65	5.71	0.028345
66	115.35	0.029648
67	4.16	0.084125
68	43.33	0.111153
69	53.13	0.022883
70	139.4	0.014065
71	170.98	0.09731
72	81.87	0.064722
73	64.98	0.025252
74	48.18	0.038893

75	116.56	0.075045
76	135	0.023731
77	7.77	0.033872
78	45	0.012944
79	130.1	0.037893
80	39.29	0.021682
81	0	0.020883
82	5.12	0.093652
83	2.07	0.115629
84	111.04	0.077565
85	36.87	0.013922
86	161.57	0.026535
87	114.78	0.090107
88	14.04	0.095143
89	113.43	0.068588
90	75.96	0.01328
91	7.13	0.103873
92	77.01	0.042973
93	55.01	0.039317
94	45	0.059217
95	0	0.170711
96	19.65	0.047883
97	113.2	0.04906

Appendix 2 - Data for Fracture Patterns and Morphology

Minkowski densities for PPS images.

ID	Image	Area Density	Perimeter Density	Euler Density	Credit
1	unit1.2.1	0.78309	0.036824	9.40E-05	NASA/JPL-CALTECH/Caltech/MSSS
2	unit1.1.1	0.6585	0.057672	0.00037	NASA/JPL-CALTECH/Caltech/MSSS
3	001474_2520_1a	0.70924	0.18051	-0.00411	NASA/JPL-CALTECH/University of Arizona
4	001474_2520_1b	0.59173	0.18255	-0.00073	NASA/JPL-CALTECH/University of Arizona
5	001474_2520_1c	0.63399	0.1895	-0.00158	NASA/JPL-CALTECH/University of Arizona
6	sand: bentonite 1:1 a	0.51532	0.17611	0.003793	Vogel et al. 2005 http://www.sciencedirect.com/science/article/pii/S001670610400196X
7	sand: bentonite 1:1 b	0.57029	0.18531	0.003219	Vogel et al. 2005 http://www.sciencedirect.com/science/article/pii/S001670610400196X
8	sand: bentonite 1:1 c	0.46126	0.14885	0.003382	Vogel et al. 2005 http://www.sciencedirect.com/science/article/pii/S001670610400196X
9	sand: bentonite 5:1 a	0.80352	0.18721	-0.00023	Vogel et al. 2005 http://www.sciencedirect.com/science/article/pii/S001670610400196X
10	sand: bentonite 5:1 b	0.77739	0.17524	0.000752	Vogel et al. 2005 http://www.sciencedirect.com/science/article/pii/S001670610400196X
11	sand: bentonite 5:1 c	0.79869	0.19085	-0.00097	Vogel et al. 2005 http://www.sciencedirect.com/science/article/pii/S001670610400196X
12	Mullins permafrost 1	0.85971	0.08516	-0.00154	Bernard Hallet
13	Mullins permafrost 2	0.83698	0.08198	-0.00067	Bernard Hallet
14	Mullins ice 1	0.63317	0.14211	0.000978	Bernard Hallet
15	farnell_ice_cement_1	0.8425	0.024017	-7.16E-05	Ron Sletten
16	farnell_ice_cement_2	0.78163	0.028464	-3.42E-05	Ron Sletten
17	farnell_ice_shallow_1	0.76759	0.019764	-3.54E-06	Ron Sletten
18	farnell_ice_shallow_2	0.74994	0.021143	-9.41E-07	Ron Sletten
19	dead sea	0.8647	0.04441	-0.00035	Weinberger 2001 http://gsabulletin.gsapubs.org.offcampus.lib.washington.edu/content/113/1/20.full.pdf
20	unspecified mud	0.91712	0.094059	-0.00123	Royalty-free @ http://thumbs.dreamstime.com/thumblarge_583/1297805186q8ZuHJ.jpg terms of use: http://www.cselandscapearchitect.com/terms-of-use/
21	racetrack 1	0.86839	0.13631	-0.0011	C. E. Jones http://www.pitt.edu/~cejones/GeoImages/5SedimentaryRocks/SedStructures/Mudcracks.html
22	racetrack 2	0.90914	0.10122	-0.00236	W. P. Armstrong http://waynesword.palomar.edu/dv7.htm
23	red lake	0.88264	0.11478	-0.00217	David Minton http://www.lpl.arizona.edu/~daminton/DV2006/Day_1_files/IMG_3851.jpg
24	romainville	0.84086	0.13885	0.000784	Tang et al. 2011 http://www.sciencedirect.com.offcampus.lib.washington.edu/science/article/pii/S0016706111002205?np=y

Appendix 3 - Data for Small Window Test

Small window test of Minkowski perimeter densities.

ID	Image	Large Window Perimeter Density	Small Window Perimeter Density	Notes
1	Farnell ice cement 1	0.024017	0.023867	Small window approx. 10 polygons, matching Glenelg window.
2	Farnell ice cement 2	0.028464	0.028855	Small window approx. 10 polygons, matching Glenelg window.
3	Farnell ice shallow 1	0.019764	0.019763	Small window approx. 10 polygons, matching Glenelg window.
4	Farnell ice shallow 2	0.021143	0.019066	Small window approx. 10 polygons, matching Glenelg window.

Appendix 4 - Minkowski Densities

Method

Vogel et al. [2005] quantified desiccation fracture patterns first with Minkowski functionals, which are fundamental properties of a spatial object [Ohser and Mücklich, 2000]. By Hadwiger's Theorem [Hadwiger, 1957] the properties of functionals are complete in the sense that all other motion invariant, continuous and additive properties can be composed of functionals. Functionals are therefore highly descriptive of the object, and useful for characterization.

For a planar object (X) such as a fracture pattern, three Minkowski functionals (W_0, W_1 and W_2) can satisfy Hadwiger's Theorem [Ohser and Mücklich, 2000], and these Minkowski functionals can be calculated from geometric and topological properties of X [Michielsen et al., 2003]:

$$W_0 = A(X)$$

$$W_1 = L(X) / 2$$

$$W_2 = \pi \chi (X)$$

Where:

A(X) is the area of object (X), i.e., the area of the planar image of fractures.

L(X) is the perimeter of object (X), i.e., the perimeter of the fractures.

χ (X) is the Euler characteristic of object (X), a measure of connectivity, i.e., the number of isolated fracture objects minus the number of holes within these objects.

For digital images the Minkowski functionals are calculated by pixel decomposition into vertices, n_0, edges, n_1, and faces, n_2 [Michielsen et al., 2003; Allen et al., 2009]:

$$W_0 = n_2$$

$$W_1 = (-4\, n_2 + 2\, n_1) / 2$$

$$W_2 = \pi\, (\, n_2 - n_1 + n_0\,)$$

The calculation of Minkowski functionals can be illustrated following Michielsen et al. [2003] with an example digital pattern (Fig. 23).

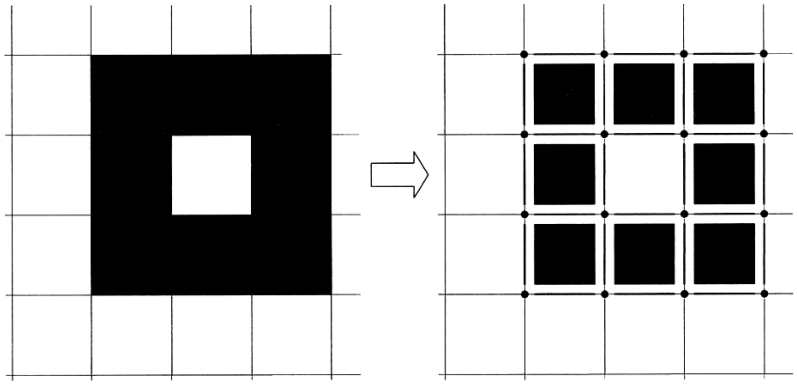

Figure 23. Decomposition of black pattern pixels into vertices (dots), edges (lines) and faces (squares) [Michielsen et al., 2003].

In Fig. 23 the object is decomposed into black pixels, which are further decomposed into 16 vertices, 24 edges and 8 faces. Calculating the Minkowski functionals for this image:

$$W_0 = 8$$

$$W_1 = (-32 + 48) / 2 = 8$$

$$W_2 = \pi\, (\, 8 - 24 + 16\,) = 0$$

To produce Minkowski densities that are independent of image size, and enable direct comparison of images of different sizes, each image's Minkowski functionals are divided by the total area of the image [Roth et al., 2005]. A practical computation of each

Minkowski density is detailed in [Legland et al., 2007] and implemented by Legland in Matlab code [Legland, 2011]. In this study Legland's code was run on Matlab 7.9.0.529. Photographs were converted to binary black-and-white images by adjustment of contrast, luminance level and threshold in Photoshop 13.0.1.

Results

Minkowski densities for two sites in the Glenelg PPS (Unit 1a, Unit 1b) and for terrestrial analogs where PPS is known to be due to thermal contraction or desiccation are plotted in Fig. 24. Permafrost PPS images were from Mullins Valley and Farnell Valley, Antarctica, and near the Phoenix landing site, Mars. Desiccation PPS images were from the Dead Sea region in Israel, Racetrack and Red Lake Playas in California, U.S.A., laboratory experiments, and one unspecified mud puddle. Please see Appendix 2 for image credits.

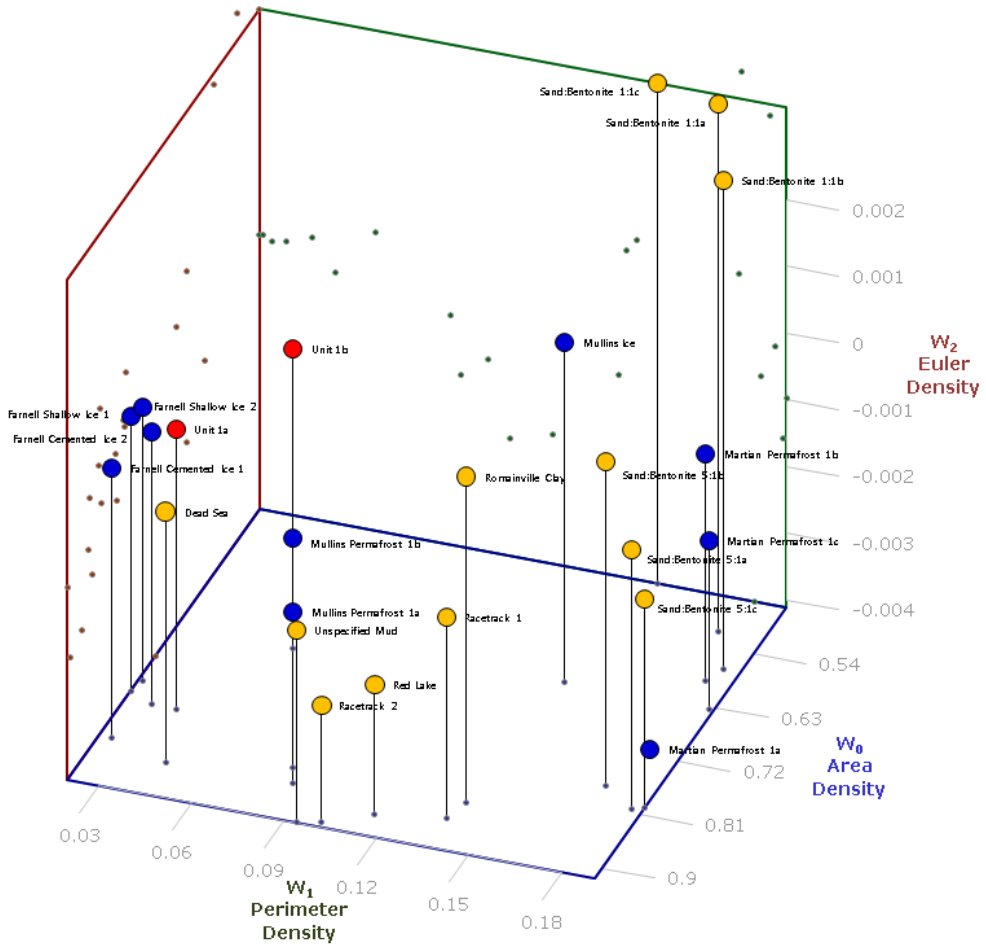

Figure 24. Minkowski densities for Glenelg PPS (red circles), thermal contraction PPG (blue circles) and desiccation PPS (yellow circles).

In Fig. 24, area density (AD) is plotted along the axis to lower right, perimeter density (PD) is axis to lower left, and Euler density (ED) is vertical axis. Characteristic values (clusters) of Minkowski densities are observed for several sets of images: e.g., for Mullins Valley permafrost images 1a and 1b, and for Racetrack Playa desiccation images 1 and 2. However, AD, PD and ED values overlap among Glenelg, thermal contraction and desiccation PPS. Notably, PD overlaps suggest that PD is not diagnostic of the mechanism causing contraction, contrary to the speculation of Vogel et al [2005]. Fig.

25 shows that Glenelg PD values are within the range of both desiccation and thermal contraction PD.

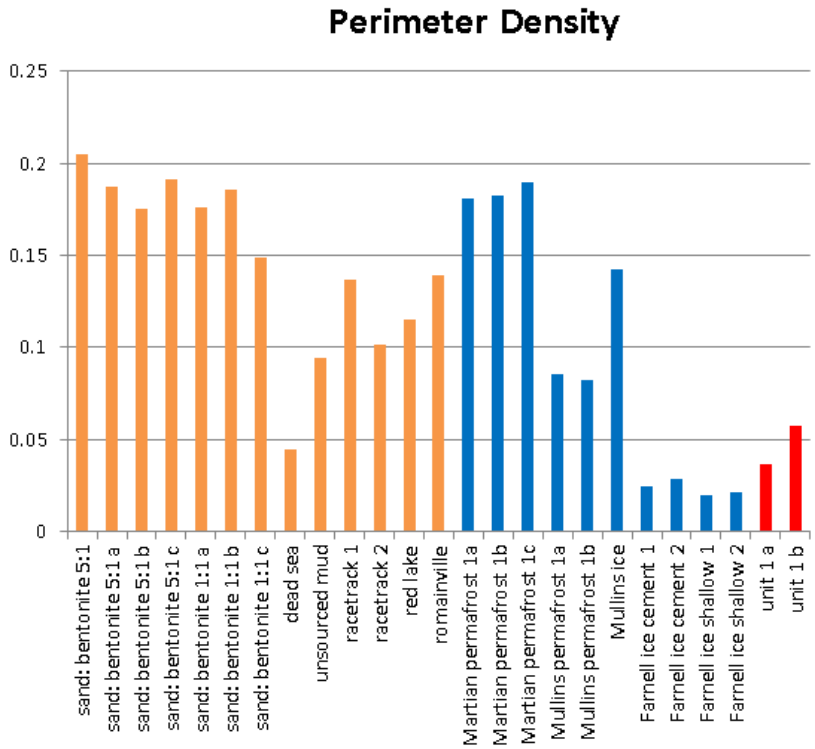

Figure 25. Perimeter densities (PD) from Fig. 24. Glenelg PPS (red), thermal contraction PPG (blue), and desiccation PPS (yellow).

There are several sources of error in PD measurement in this analysis. At Glenelg the Minkowski functional analysis was constrained by the available imagery. Imagery with sufficient resolution and area coverage for Minkowski measurements was available for only two Glenelg PPS sites, making the sample population very small. Also "cleaning" of images was required to remove shadows and low-contrast debris that mimicked fractures in the binary image pattern. Cleaning was performed manually, with judgments by eye, using both projected and raw imagery. Moreover, fracture walls

were not perfectly vertical, and some were degraded. Fractures were often completely filled with loose sandy material that may have decreased the apparent PD. Collectively, these limitations introduced errors into the Glenelg PD measurements, and in satellite images of martian permafrost, which frequently contained ambiguous shadows and low-contrast debris. Fracture fill was likely the largest source of error in Glenelg PD. All errors in Glenelg PPS PD measurements are estimated to total less than 15%. For PD measurements of martian PPG, fracture fill and lower HiRISE image resolution produced errors totaling perhaps 25%. Smaller errors, totaling perhaps 10%, are estimated for PD measurements of images of terrestrial PPS.

The small viewing window imposed on Glenelg PPS images raises another potential source of error. Each planar-projected Glenelg PPS image includes only a small number of polygons (<10). To test for potential effects of small window size on PD values, images of terrestrial PPS with many polygons were cropped to about 10 polygons so as to match Glenelg PPS images, and Minkowski densities were calculated for these small-window images. Small-window PD values are shown to be similar to large-window (>30 polygons) PD values in Fig. 26.

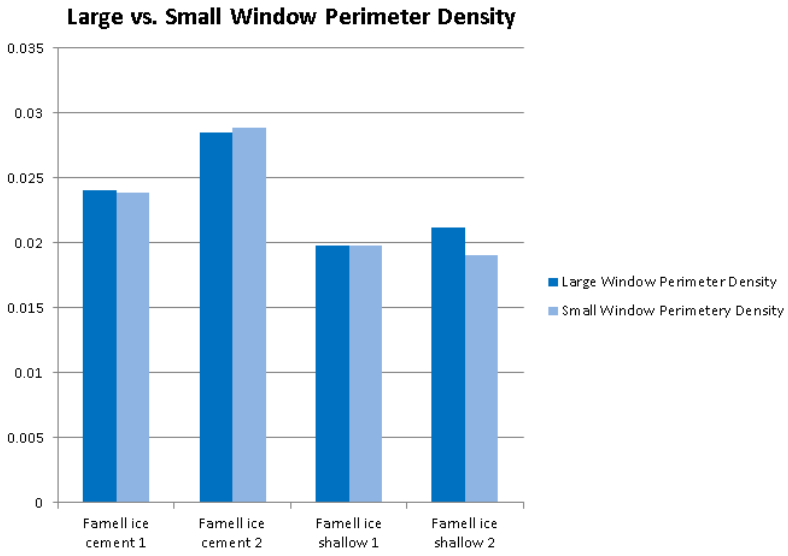

Figure 26. Large vs. small window PD for Farnell Valley, Antarctica.

As seen in Fig. 26, the small window produced no significant change in PD values.

Please see Appendix 3 for details.